Journal of the Turkish Chemical Society Section: A Chemistry
Turkish Chemical Society

Evaluation of Structural and Dielectric Properties of Eu^{3+}, B^{3+} co-doped Ba_2GdMO_6 (M=Nb, Ta) Double Perovskite Ceramics

Mustafa İlhan[1*], Lütfiye Feray Güleryüz[2]

[1]Department of Environmental Engineering, Faculty of Engineering, Marmara University, Maltepe, 34854, İstanbul, Türkiye.
[2]Department of Tobacco Technology Engineering, Manisa Celal Bayar University, Akhisar 45200, Manisa, Türkiye.

Abstract: In the study, the structural and dielectric properties of Ba_2GdMO_6 (M=Nb, Ta) double perovskite ceramics produced with solid-state method were examined by co-doping $x$$Eu^{3+}$ and $y$$B^{3+}$ (x=10 mol%, y=0, 5, 15, 30, 50, 70 and 100 mol%). XRD (X-ray diffraction) results of the ceramic samples exhibited a single-phase structure with cubic symmetry *Fm*-3*m* space group, while increasing B^{3+} concentration led to an increase in crystallite sizes and lattice parameters up to 50 mol% in both series. SEM (scanning electron microscopy) examinations revealed the presence of boron-supported grain growth and agglomeration in the grains of both series, and also a slight angularity occurred in grain shape at high B^{3+} concentrations. The dielectric constant (ε') of the ceramic samples in both series increased with increasing boron concentration up to 50 mol%, and it was approximately 33.5 and 35.4 at 20 Hz for the $Ba_2Gd_{1-x}NbO_6{:}xEu^{3+}, yB^{3+}$ and $Ba_2Gd_{1-x}TaO_6{:}xEu^{3+}, yB^{3+}$, respectively. The decrease in the dielectric constant after 50 mol% may be attributed to the presence of increased strain in the structure, as shown by the decrease in crystallite size. The increasing B^{3+} concentration caused a decrease in dielectric loss (tan δ) in both series, which was attributed to the suppression of oxygen vacancies due to the increased presence of B^{3+} and hence to a decrease in ionic conductivity and dielectric loss.

Keywords: Ba_2GdNbO_6; Ba_2GdTaO_6; Eu^{3+}, B^{3+} co-doping; dielectric properties.

Submitted: February 28, 2024. **Accepted:** May 20, 2024.

Cite this: İlhan M, Güleryüz LF. Evaluation of Structural and Dielectric Properties of Eu^{3+}, B^{3+} co-doped Ba_2GdMO_6 (M=Nb, Ta) Double Perovskite Ceramics. JOTCSA. 2024;11(3): 1099-110.

DOI: https://doi.org/10.18596/jotcsa.1444484

***Corresponding author's E-mail:** mustafa.ilhan@marmara.edu.tr

1. INTRODUCTION

The $A_2BB'O_6$ type double perovskite structure attracts the attention of material scientists and solid-state chemists. This interest stems from their dielectric properties, such as low dielectric loss, and low chemical reactivity, as well as their potential applications, such as their compatibility with some of the commonly used superconductors as a result of having a suitable coefficient of thermal expansion (1-6). The double perovskites with the general formula $A_2B'B''O_6$ are formed when the B site of ABO_3 is occupied by two different cations (B′ = rare earth elements, B″ = transition metal, d-block metals, such as Nb, Ta, Mo, Sb) in the disordered state (7,8). Perovskite oxides with the structure ABO_3, which contain two different cations represented as A and B, are structurally stable due to the balanced arrangement of the constituent atoms and valences. Moreover, when the B site is occupied by a transition metal, $B'O_6$ and $B'O_6$ in $A_2B'B'O_6$ perovskite can reduce the symmetry of the A sites and become suitable hosts for doping rare earth ions to obtain luminescent ferroelectrics (9-16). On the other hand, investigating the electrical properties of ferroelectric materials doped with trivalent europium ion (Eu^{3+}) is important for the development of versatile optoelectronic devices (17-19). The Eu^{3+} is known for its strong luminescence in the red spectral region. It exhibits interesting spectral properties with $^5D_0 \rightarrow {}^7F_J$ (J=0, 1, 2, 3, 4, 5, 6) transitions, as well as having non-degenerate (J=0) first levels of transitions in both the absorption and luminescence spectrum, and has a great advantage over other RE ions (20-25). Boron is extensively employed as a flux in traditional solid-state reactions due to its relatively low melting point. Additionally, it's utilized to enhance optical and dielectric properties, alongside influencing structural aspects like morphology and crystallinity (26-29). Additionally, there are studies on the effect of boron on grain morphology and its improvement in dielectric properties in which the doping of boron has the effect of increasing the bulk properties to some extent and can reduce the grain boundaries in the structure (30-32).

In the study, the structural and dielectric properties of Eu^{3+} doped Ba_2GdMO_6 (M=Nb, Ta) ceramics were studied by B^{3+} co-doping. The structural and dielectric characterizations of ceramic samples were carried out by XRD, SEM, and impedance analyses.

2. EXPERIMENTAL

$Ba_2Gd_{1-x}NbO_6$:xEu^{3+}, yB^{3+} (x=10 mol%, y=0, 5, 15, 30, 50, 70 and 100 mol%) and $Ba_2Gd_{1-x}TaO_6$:xEu^{3+}, yB^{3+} (x=10 mol%, y=0, 5, 15, 30, 50, 70 and 100 mol%) ceramic samples were fabricated by solid-state reaction. Barium carbonate $BaCO_3$ (Sigma-Aldrich, 99%), niobium oxide (Nb_2O_5: Alpha Aesar, 99.9%), tantalum oxide (Ta_2O_5: Alpha Aesar, 99.9%) powders and gadolinium oxide (Gd_2O_3: Alpha Aesar, 99.9%) were used as starting materials in calculated stoichiometric amounts. Europium oxide (Eu_2O_3: Alpha Aesar, 99.9%) and boric acid (H_3BO_3: Kimyalab, %99.9) were used as dopant materials. The stoichiometric amounts of $Ba_2Gd_{0.9}NbO_6$:$0.1Eu^{3+}$ and $Ba_2Gd_{0.9}TaO_6$:$0.1Eu^{3+}$ starting materials were weighed and mixed in an agate mortar to provide homogeneity. Then, by adding different amounts of boric acid (H_3BO_3), the final mixture of the powders was thoroughly mixed and ground in an agate mortar for the last time to provide more homogeneity. For sintering process, the sufficient amount of mixture was taken and calcined in an alumina crucible at 1250 °C for 6 h after pelleting.

The phase structure of the samples were examined by XRD (X-ray diffractometer; D2 PHASER, Bruker Corp., Germany) using Cu-K_α (1.5406 Å) radiation in between 2θ=15-80 °C with scan speed 2 °C/min. The grain morphology of the samples was investigated by scanning electron microscopy (FEG-SEM; XL 30S, Philips Corp., Netherlands). The crystal structure was visualized via VESTA software. The average crystallite sizes of the samples were determined from the Scherrer Eq. (1) (33):

$$D = \frac{k \cdot \lambda}{B \cdot \cos\theta} \quad (1)$$

where D stands for particle size in nanometers, with k is a constant (usually taken as 0.9). CuKα represents the wavelength (λ = 0.15406 Å), and B is the full width at half maximum in radians. Frequency-dependent changes of real and imaginary permittivity and loss factor were defined using dielectric Eq. (2) and Eq. (3) respectively:

$$\varepsilon' = \frac{C}{C_0}, \qquad \varepsilon'' = \frac{G}{\omega C_0}, \qquad C_0 = \varepsilon_0 \frac{A}{d} \quad (2)$$

$$\tan\delta = \frac{\varepsilon''}{\varepsilon'} \quad (3)$$

where C_0 is vacuum capacitance, C is capacitance, w is angular frequency and G is conductance. The dielectric properties of the ceramic samples were carried out using an impedance analyzer (HIOKI, LCR Hitester 3532-50; between frequency 20 Hz–10^6 Hz, UK) at room temperature.

3. RESULTS AND DISCUSSION

3.1. XRD-SEM Results of $Ba_2Gd_{1-x}NbO_6$:xEu^{3+}, yB^{3+} and $Ba_2Gd_{1-x}TaO_6$:xEu^{3+}, yB^{3+}

Figure 1a and Figure 2a show the XRD results for $Ba_2Gd_{1-x}MO_6$:xEu^{3+}, yB^{3+} (M=Nb, Ta), (x=10 mol%, y=0, 5, 15, 30, 50, 70, 100 mol%) samples, respectively. X-ray diffractions of all the sintered samples from 0 to 100 mol% B^{3+} showed the single-phase of Ba_2GdMO_6 (M=Nb, Ta). The crystal structure of Ba_2GdNbO_6 (JCPDS card no. 47-0378) and Ba_2GdTaO_6 (JCPDS card no. 49-1900) was indexed with space group $Fm\bar{3}m$ (225) and cubic symmetry. Figure 3 shows the schematic representation of Ba_2GdMO_6 (M=Nb, Ta) crystal structure consisting of edge-shared $B'O_6$ (GdO_6) and $B''O_6$ (MO_6) octahedral, where the formation of the single-phase or the absence of any minor phase may be explained to the substitution of Eu^{3+} ions with ionic radius 0.947 Å (for 6 CN) by Gd^{3+} ions (r=0.938 Å, for 6 CN), and the dissolution of the boron co-doped at different concentrations in double perovskite host. Figure 1b and Figure 2b shows XRD two theta angles (400) for $Ba_2Gd_{1-x}NbO_6$:xEu^{3+}, yB^{3+} and $Ba_2Gd_{1-x}TaO_6$:xEu^{3+}, yB^{3+}, respectively, where the XRD two theta peaks shifted towards smaller angles. Considering the slightly larger ionic radius of Eu^{3+}, the substitution of Gd^{3+} with Eu^{3+} would contribute to lattice expansion. In addition, B^{3+} ions, which are characterized by a small ionic radius and are likely to occupy the structure as interstitial atoms, can lead to the expansion of the lattice. Table 1 summarizes the variation of lattice data and crystallite size. The shift is related to the increase in the lattice constant which elevates up to 100 mol% B^{3+} concentration in both series. The cell data (a, V) for 0 and 100 mol% B^{3+} concentrations were 8.4729 Å, 608.27 Å^3 and 8.5029 Å, 614.75 Å^3 respectively, for $Ba_2Gd_{1-x}NbO_6$:xEu^{3+}, yB^{3+}, while they were 8.4680 Å, 607.22 Å^3 and 8.4942 Å, 612.87 Å^3, respectively, for $Ba_2Gd_{1-x}TaO_6$:xEu^{3+}, yB^{3+}. The lattice parameters Ba_2GdNbO_6 (34) and Ba_2GdTaO_6 (35) compounds are a=8.4900 Å, V=611.96 Å^3 and a=8.4780 Å, V=609.37 Å^3, respectively. The cell data had values close to the literature data, where the lattice volume increased by about 1% in both series.

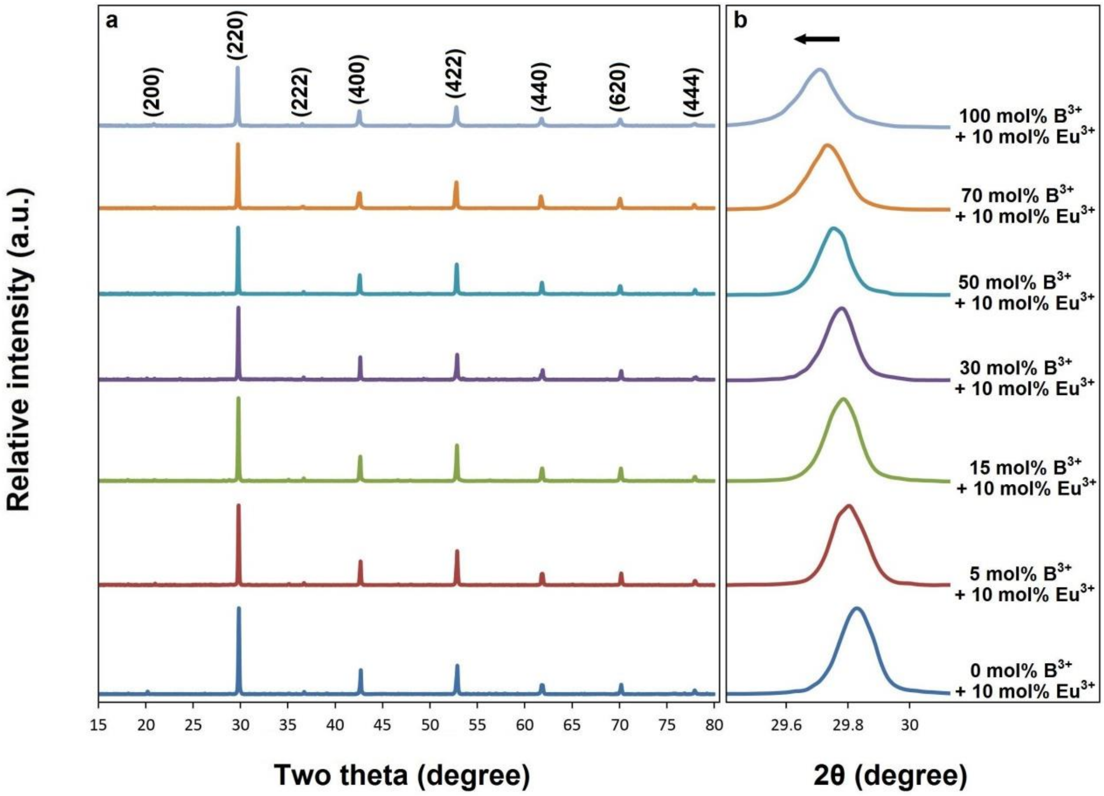

Figure 1: (a) X-ray diffractions of $Ba_2Gd_{1-x}NbO_6$:$x$$Eu^{3+}$, $y$$B^{3+}$ co-doped ceramics (x=10 mol%, and y= 0, 5, 15, 30, 50, 70 and 100 mol%), (b) XRD two theta peak (400) shifted to lower angles with B^{3+} concentration.

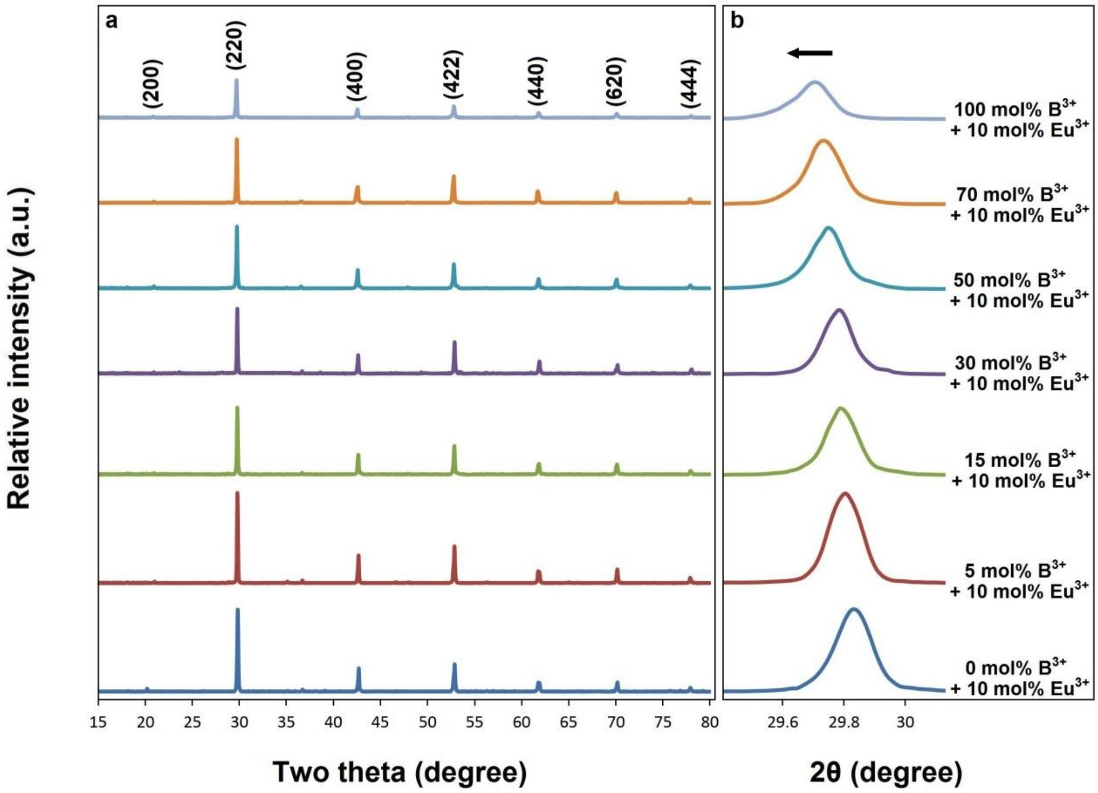

Figure 2: (a) X-ray diffractions of $Ba_2Gd_{1-x}TaO_6$:$x$$Eu^{3+}$, $y$$B^{3+}$ co-doped ceramics (x=10 mol%, and y= 0, 5, 15, 30, 50, 70 and 100 mol%), (b) XRD two theta peak (400) shifted to lower angles with B^{3+} concentration.

The average crystallite sizes of the samples determined from the Scherrer equation using two theta reflection peaks (220), (400) and (422) are summarized in Table 1. The increasing B^{3+} concentration led to an increase in crystallite size in both series up to range of 30-50 mol%, and then a decrease occurred at 70 and 100 mol% concentrations. As seen in Table 1, the crystallite sizes from 0 to 50 mol% B^{3+} varied to 42.36-49.14 nm for $Ba_2Gd_{1-x}NbO_6$:$x$$Eu^{3+}$, $y$$B^{3+}$, while the sizes changed in the same range as 47.07-55.61 nm for $Ba_2Gd_{1-x}TaO_6$:$x$$Eu^{3+}$, $y$$B^{3+}$, respectively. However, increasing boron concentration caused a decrease in crystallinity size at 70 and 100 mol% levels, where the crystallite sizes for 70 and 100 mol% B^{3+} concentrations were 45.79 and 43.38 nm (for $Ba_2Gd_{1-x}NbO_6$:$x$$Eu^{3+}$, $y$$B^{3+}$) and 49.72 and 46.28 nm (for $Ba_2Gd_{1-x}TaO_6$:$x$$Eu^{3+}$, $y$$B^{3+}$), respectively. Since the temperature effect will increase with increasing boron, the nucleation rate will slow down, which is related to the increasing crystallite size in the 0-50 mol% range. On the other hand, the decrease in crystallite size at 70 and 100 mol% can be linked to elevated boron concentration, leading to heightened nucleation, lattice deformation, and disruption of the charge balance within the structure, particularly at higher levels of doping (36-38).

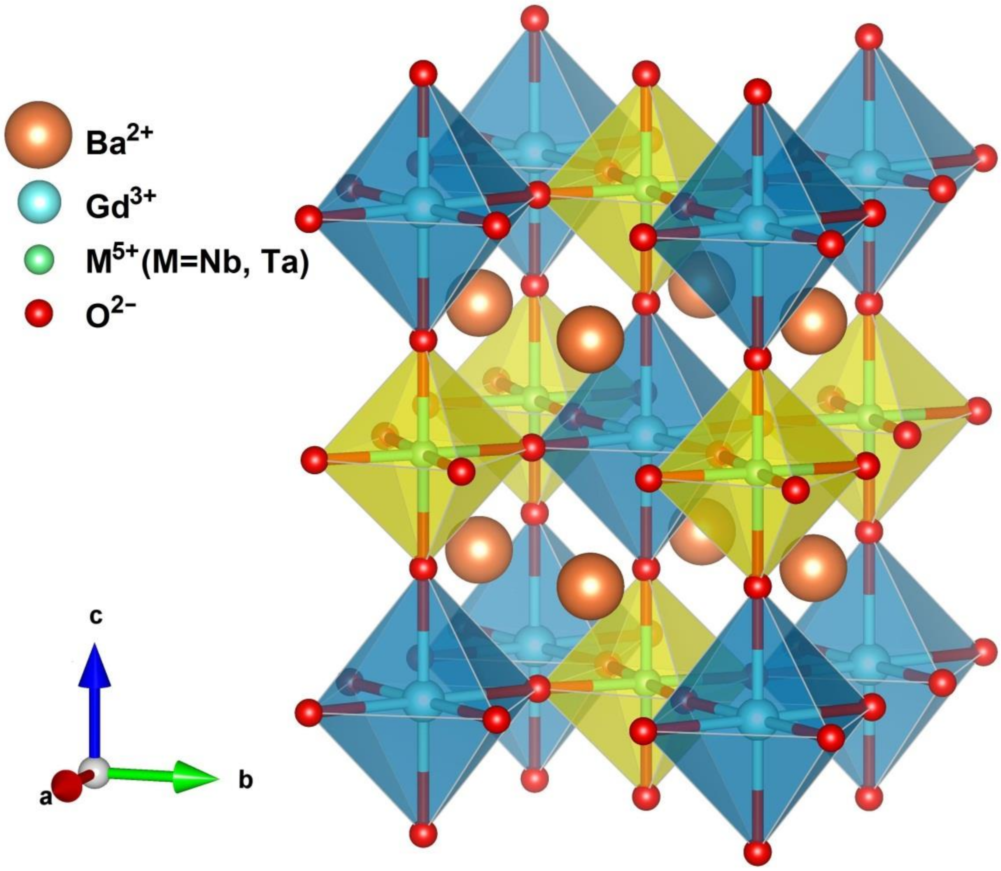

Figure 3: Crystal structure visualization of Ba_2GdMO_6 (M=Nb, Ta).

Table 1: Lattice parameters (a, V) and average crystallite sizes (D) for $x$$Eu^{3+}$, $y$$B^{3+}$ co-doped $Ba_2Gd_{1-x}NbO_6$ and $Ba_2Gd_{1-x}TaO_6$ ceramics.

Sample concentration (mol%)	**$Ba_2Gd_{1-x}NbO_6$:$x$$Eu^{3+}$, $y$$B^{3+}$**			**$Ba_2Gd_{1-x}TaO_6$:$x$$Eu^{3+}$, $y$$B^{3+}$**		
	***a* (Å)**	***V* (Å³)**	***D* (nm)**	***a* (Å)**	***V* (Å³)**	***D* (nm)**
0 B^{3+}, 10 Eu^{3+}	8.4729	608.27	42.36	8.4680	607.22	47.07
5 B^{3+}, 10 Eu^{3+}	8.4804	609.88	43.78	8.4717	608.02	48.08
15 B^{3+}, 10 Eu^{3+}	8.4841	610.69	46.57	8.4792	609.63	51.79
30 B^{3+}, 10 Eu^{3+}	8.4879	611.50	49.11	8.4830	610.44	55.92
50 B^{3+}, 10 Eu^{3+}	8.4954	613.12	49.14	8.4904	612.06	55.61
70 B^{3+}, 10 Eu^{3+}	8.4991	613.93	45.79	8.4867	611.25	49.72
100 B^{3+}, 10 Eu^{3+}	8.5029	614.75	43.38	8.4942	612.87	46.28

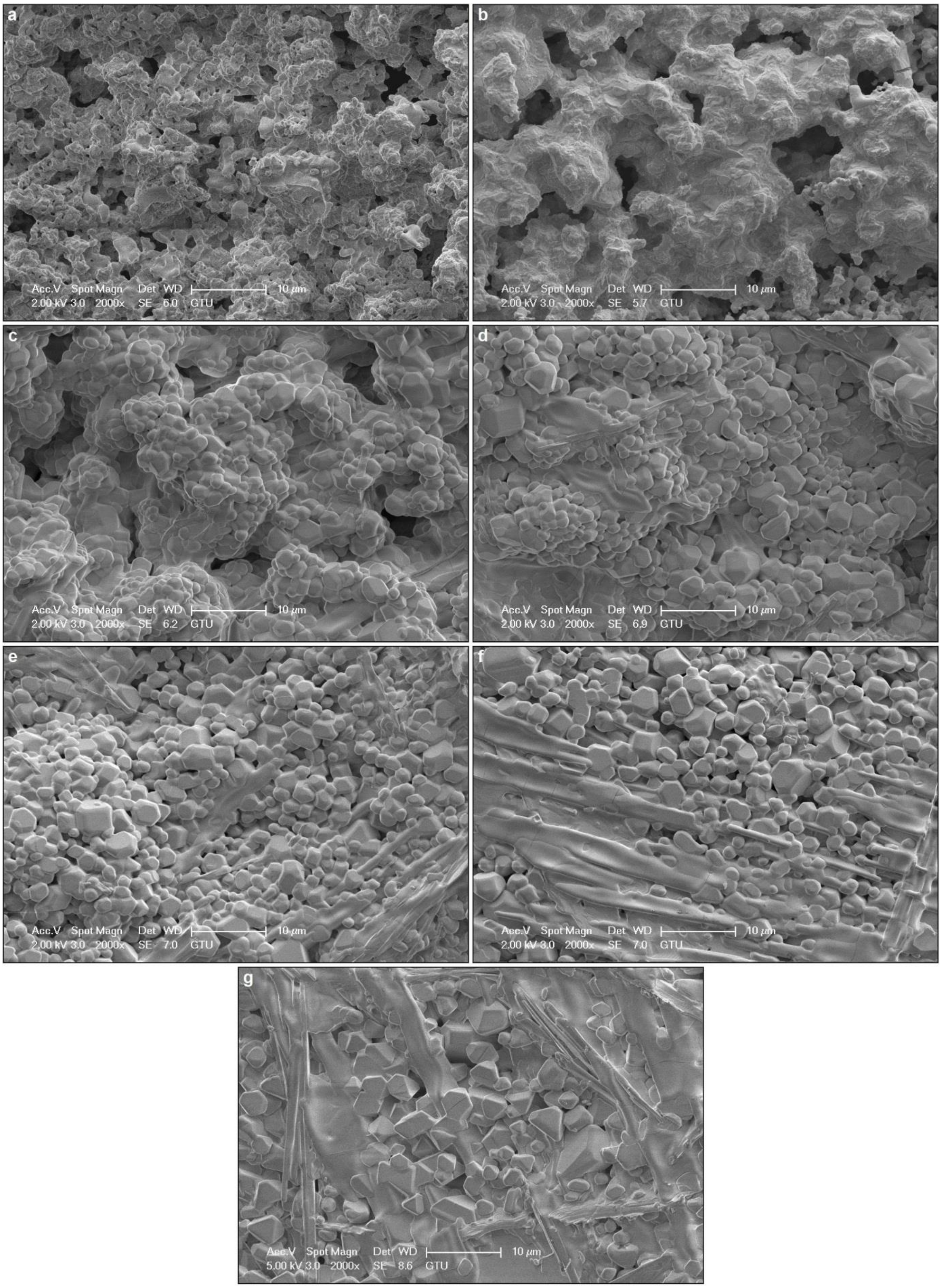

Figure 4: SEM micrographs of 10 mol% Eu^{3+} and (a) 0, (b) 5, (c) 15, (d) 30, (e) 50, (f) 70 and (g) 100 mol% B^{3+} co-doped Ba_2GdNbO_6 ceramics, at 2000× magnification and 2 kV acceleration voltage.

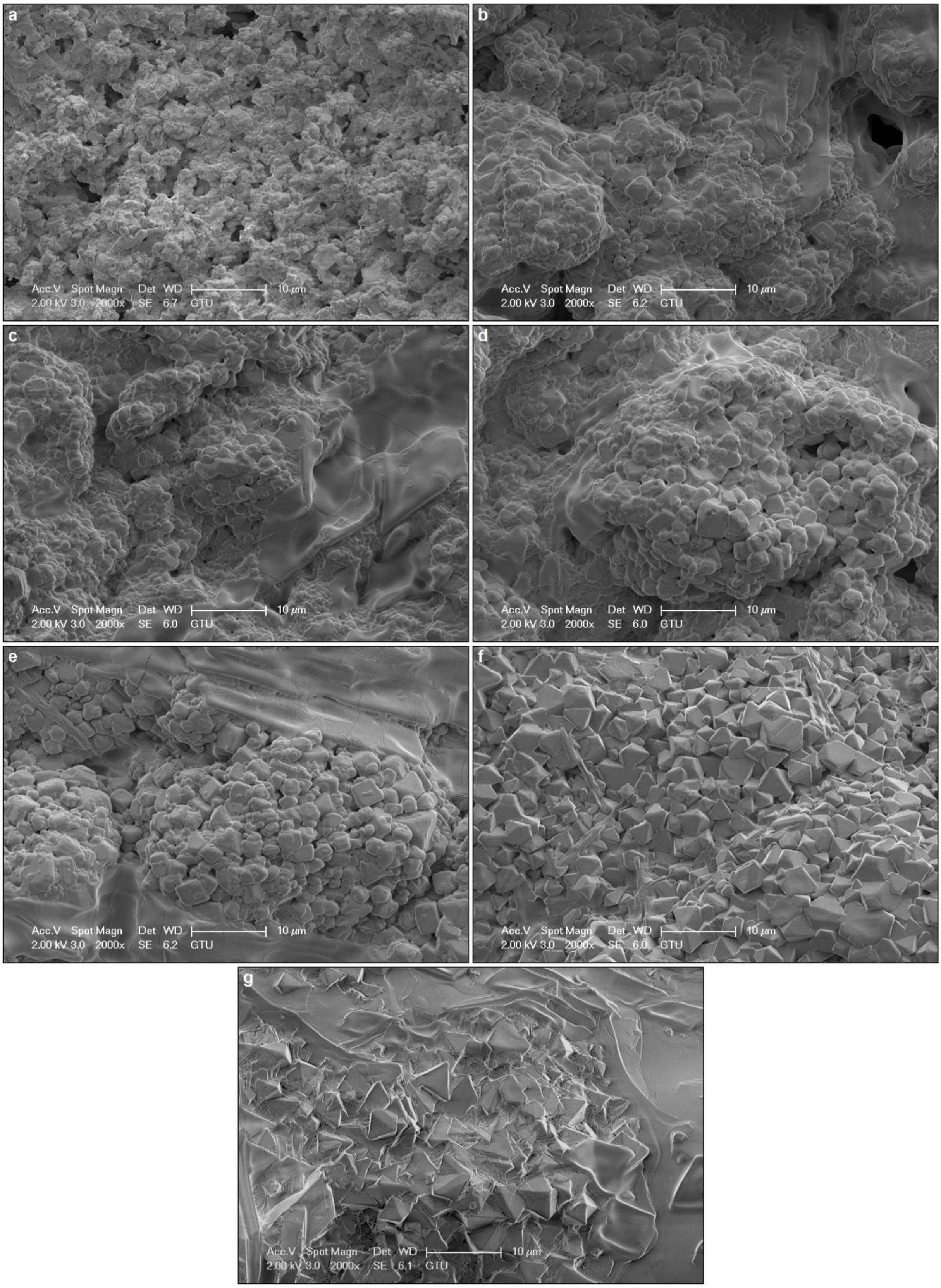

Figure 5: SEM micrographs of 10 mol% Eu^{3+} and (a) 0, (b) 5, (c) 15, (d) 30, (e) 50, (f) 70 and (g) 100 mol% B^{3+} co-doped Ba_2GdTaO_6 ceramics, at 2000× magnification and 2 kV acceleration voltage.

Figure 4(a-g) and Figure 5(a-g) show the SEM micrographs of $Ba_2Gd_{1-x}NbO_6$:$x$$Eu^{3+}$, $y$$B^{3+}$ and $Ba_2Gd_{1-x}TaO_6$:$x$$Eu^{3+}$, $y$$B^{3+}$ (x=10 mol%, y=0, 5, 30, 50, 70 and 100 mol%) samples, respectively, at 2000× magnifications under 2 kV accelerating voltage. SEM micrographs of both series have an irregular shape and the grains are rounded, while the increasing B^{3+} concentration led to grain growth and agglomeration. As well-known boron's flux effect reduces sintering temperature. Consequently, the increase in grain size may be attributed to the elevated temperatures resulting from boron addition. This higher temperature facilitates the release of stored energy within the grains, leading to an increase in grain size (39,40). In addition, as seen in Figure 4(f,g) and Figure 5(f,g), the grain shape showed a slight angular trend at high B^{3+} concentrations. Moreover, at a concentration of 100 mol% B^{3+}, the agglomeration and flux effect is evident in the grains (Figure 4g and Figure 5g). The grain size of $Ba_2Gd_{1-x}NbO_6$:$x$$Eu^{3+}$, yB^{3+} samples varied mostly in the range of 0.5-2 μm at 0 mol% concentration and there are also some grains reaching 3-4 μm, while the size of large grains ranging from 3 to 6 μm, while the grain size can exceed 10 μm, at 100 mol% concentration (Figure 4(f,g)). The grain sizes of $Ba_2Gd_{1-x}TaO_6$:$x$$Eu^{3+}$, yB^{3+} samples are round-like and/or shapeless grains varied between 0.5-3 μm at 0 mol%, whilst the sizes of the angular grains at 100 mol% ranged between 4-10 μm (Figure 5(f,g)).

3.2. Dielectric Properties of $Ba_2Gd_{1-x}MO_6$:$x$$Eu^{3+}$, yB^{3+} (M=Nb, Ta), (x=10 mol%, y=0, 5, 15, 30, 50, 70 and 100 mol%) Ceramics

Figure 6(a,b) show the dielectric constants (ε') with frequency for $Ba_2Gd_{1-x}NbO_6$:$x$$Eu^{3+}$, yB^{3+} and $Ba_2Gd_{1-x}TaO_6$:$x$$Eu^{3+}$, yB^{3+} (x=10 mol%, y=0, 5, 15, 30, 50, 70 and 100 mol%) samples, respectively. In Figure 6a, the dielectric constants of $Ba_2Gd_{1-x}NbO_6$:$x$$Eu^{3+}$, yB^{3+} from 0 to 100 mol% B^{3+} changed approximately 21.3 and 33.5 at 20 Hz, respectively. In Figure 6b, at the same range and 20 Hz, the ε' values for the $Ba_2Gd_{1-x}TaO_6$:$x$$Eu^{3+}$, yB^{3+} ceramics were 21.3 and 35.4, respectively. However, the dielectric constant did not change in the high frequency or over 10^3 Hz. As the frequency rises, the electron exchange's capability to align with the applied field diminishes, leading to a reduction in the dielectric constant. At extremely high frequencies, the field reverses before the space charge carriers can respond, thereby preventing them from contributing to polarization (41-47), so the dielectric constant almost stayed unchanged at the high-frequency range. Moreover, as seen in Figure 6(a,b) there is an increase in polarization or dielectric constant from 0 to 50 mol% B^{3+}. The increase can be accounted for by the Maxwell-Wagner theory of external factors. According to this principle, the dielectric constant correlates directly with the grain size of the sample. The larger grain sizes result in greater atom polarizability, leading to an uptick in the dielectric constant (48-52). In the SEM micrographs in Figure 4(a-g) and Figure 5(a-g), it was previously noted that there is an increase in grain size with increasing B^{3+} concentration. Hence, this circumstance may be ascribed to the declining occurrence of grain boundaries in both series, coupled with the rise in polarizability and the value of ε' within the atomic structure. Additionally, although there was a slight increase in grain size at 70 and 100 mol% B^{3+} concentrations in both series, there was a decrease in dielectric constant. Caruntu et al (53) stated that there is a direct correlation between the change of dielectric constant and crystallite size/microstrain, in which the crystallite size increases uniformly from 32 to 94 nm with the increase of sintering temperature from 600 to 1000 °C. On the other hand, Kim et al (54), in their study on $BaTiO_3$ and $SrTiO_3$, found that the presence of an optimal amount of lattice distortion or strain increases the dielectric constant. However, there is no information about crystallite size change in the study. As seen in Table 1, a decrease in crystallite size occurs at 70 and 100 mol% B^{3+} concentrations. Furthermore, while there is a noticeable rise in both crystallite size and dielectric constant as the concentration increases from 0 to 50 mol%, the augmented cell constant can be attributed to alterations in charge equilibrium and the existence of strain. In this context, the decrease in dielectric constant at 70 and 100 mol% could be linked to heightened strain due to an increased cell constant and deteriorated charge balance, as evidenced by the reduction in crystallite size.

Figure 7(a,b) show the dielectric losses (tan δ) with frequency for $Ba_2Gd_{1-x}NbO_6$:$x$$Eu^{3+}$, yB^{3+} and $Ba_2Gd_{1-x}TaO_6$:$x$$Eu^{3+}$, yB^{3+} (x=10 mol%, y=0, 5, 15, 30, 50, 70 and 100 mol%) samples, respectively. As seen in Figure 7(a,b), dielectric loss continuously decreases with the increase in frequency. In the low-frequency range where resistance is high, polarization necessitates more energy because of the grain boundary. Conversely, in the high-frequency range where resistance is low, electron transfer across the grain boundary requires minimal energy, resulting in reduced energy loss (54-57). On the other hand, the dielectric loss factor for both sample series decreased with increasing B^{3+} concentration up to 50 mol% and then showed a slight increase at 70 and 100 mol%. Various studies in the literature connect the tan δ in ferroelectrics to oxygen vacancies, which contribute to the dielectric loss or leakage current (58-61). Liu et al (62) studied the dielectric loss and oxygen vacancy relation by fabricating TTB-$Ba_4Nd_2Fe_2Nb_8O_{30}$ ceramics at different annealing and sintering temperatures as well as in O_2 and N_2 atmospheres, where the increase in temperature reduces oxygen vacancies and electrical conductivity. Similarly, in the study reported by Iqbal et al (57) on $CuFe_2O_4$, an increase in crystallite size and dielectric constant occurred due to the increase in annealing temperature. The results of the flux effect of boron, as seen in the XRD-SEM section, the temperature effect on the structure will increase with increasing boron concentration. Thus, the higher concentration of boron will not only intensify the material's sensitivity to temperature but also impact the presence of oxygen vacancies. Therefore, the decrease in the dielectric loss factor in both series may be attributed to the suppression of oxygen vacancies by the temperature effect that increases with the increase in B^{3+}. In addition, the slightly increased dielectric loss at the 70 and 100 mol% levels is likely due to the high B^{3+} concentration leading to some increase in the mobility of oxygen vacancies in the structure.

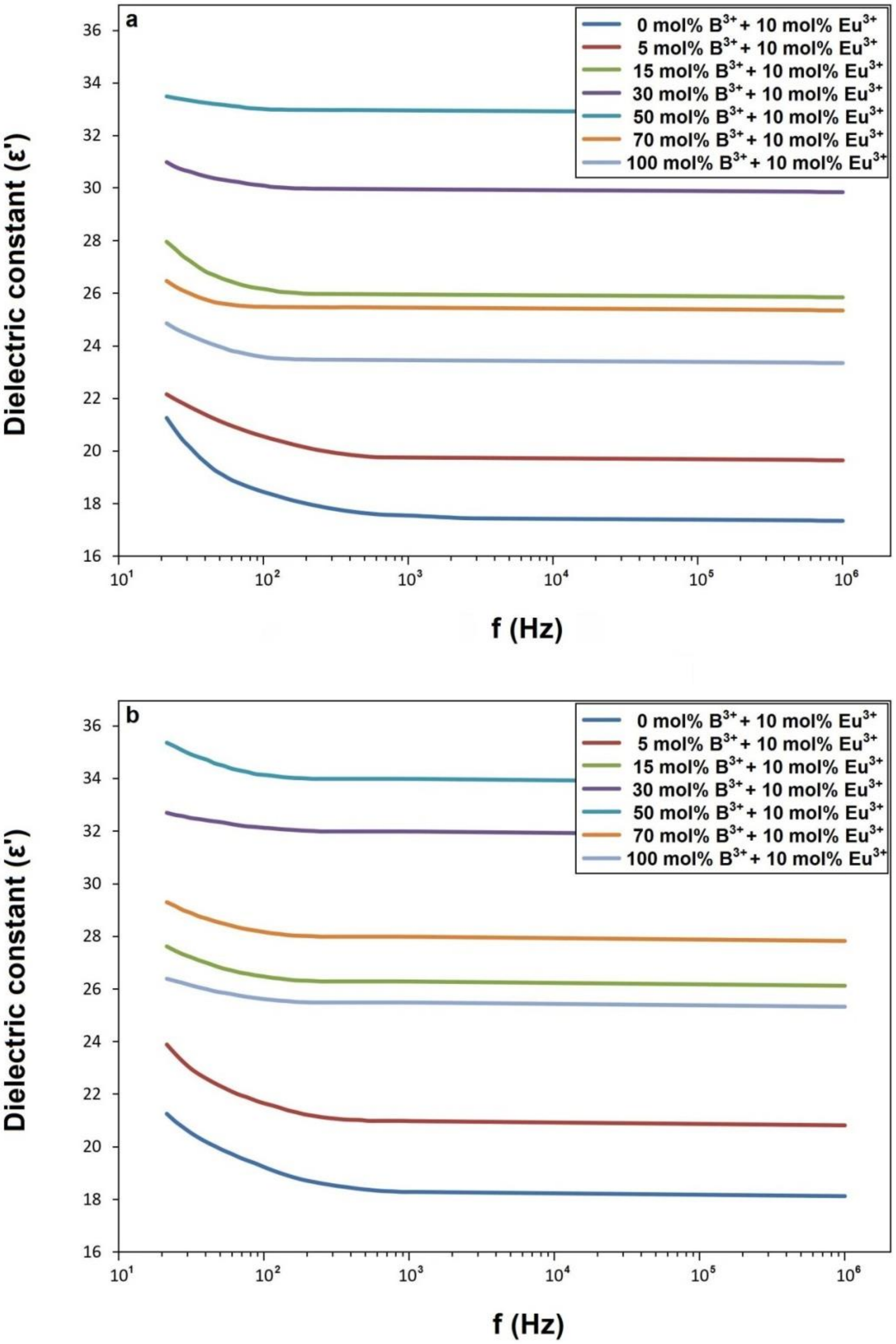

Figure 6: Dielectric constants for (a) $Ba_2Gd_{1-x}NbO_6$:$x$$Eu^{3+}$, $y$$B^{3+}$ (x=10 mol%, y=0, 5, 15, 30, 50, 70, 100 mol%), and (b) $Ba_2Gd_{1-x}TaO_6$:$x$$Eu^{3+}$, $y$$B^{3+}$ (x=10 mol%, y=0, 5, 15, 30, 50, 70, 100 mol%) ceramics.

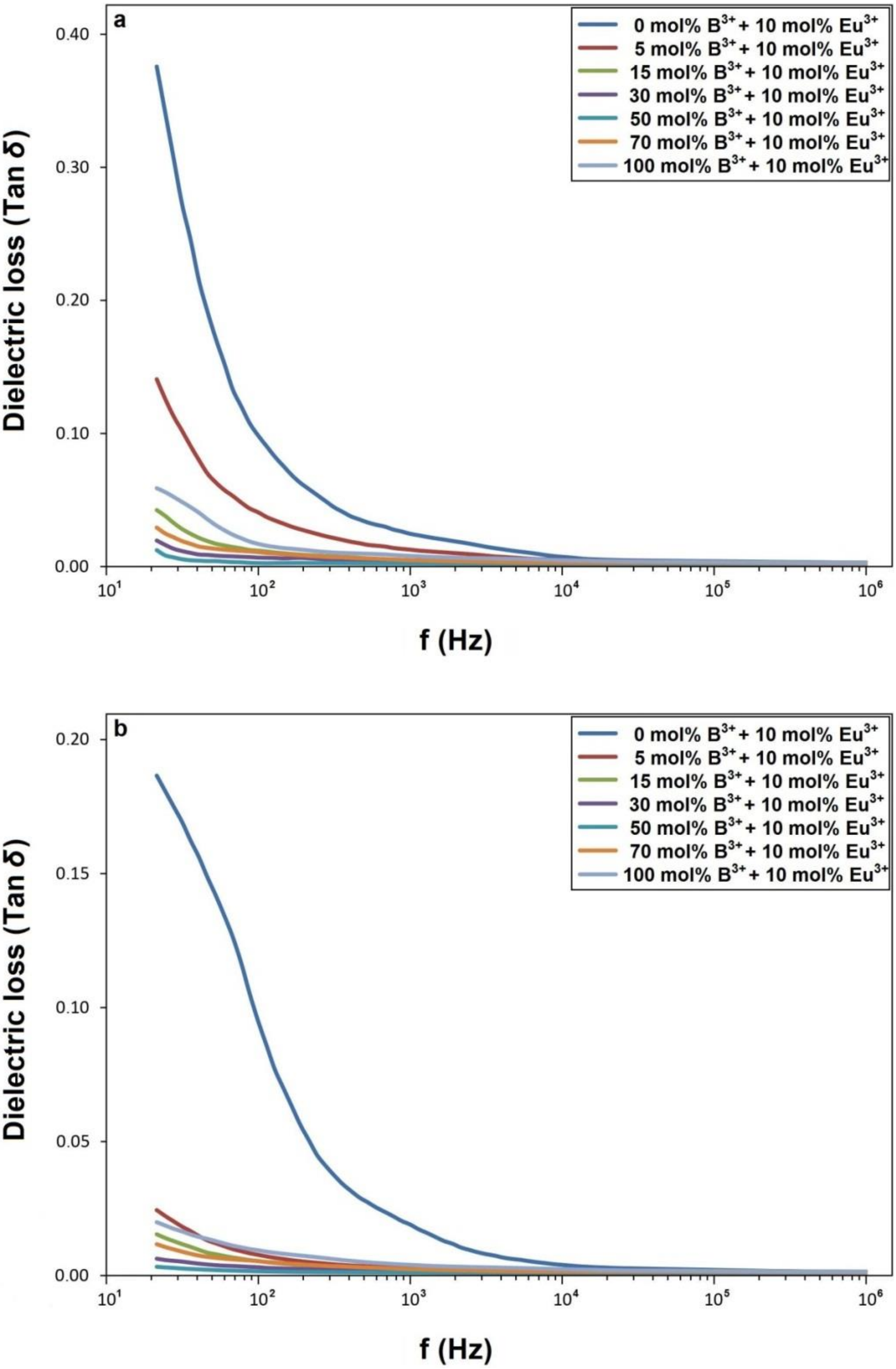

Figure 7: Dielectric losses (tan δ) for (a) $Ba_2Gd_{1-x}NbO_6$:xEu^{3+}, yB^{3+} (x=10 mol%, y=0, 5, 15, 30, 50, 70, 100 mol%), and (b) $Ba_2Gd_{1-x}TaO_6$:xEu^{3+}, yB^{3+} (x=10 mol%, y=0, 5, 15, 30, 50, 70, 100 mol%) ceramics.

4. CONCLUSION

The effect of boron on the structural and dielectric properties was studied by using Eu^{3+}, B^{3+} co-doped double perovskite $Ba_2Gd_{1-x}MO_6$:xEu^{3+}, yB^{3+} (M=Nb, Ta), (x=10 mol%, y=0, 5, 15, 30, 50, 70 and 100 mol%) ceramics, in which XRD results of the ceramics showed a single-phase structure. $Ba_2Gd_{1-x}TaO_6$:xEu^{3+}, yB^{3+} samples had slightly better crystallite sizes than $Ba_2Gd_{1-x}NbO_6$:xEu^{3+}, yB^{3+} ones, while the crystallinity of both sample series increased up to about 50 mol% B^{3+}, and then decreased at 70 and 100 mol%. SEM micrographs of Eu^{3+}, B^{3+} co-doped samples showed that boron in both series supported aggregation and growth in grains, and a slight angularity in grain shape occurred at high B^{3+} concentrations. The ε' values of $Ba_2Gd_{1-x}NbO_6$:xEu^{3+}, yB^{3+}, and $Ba_2Gd_{1-x}NbO_6$:xEu^{3+}, yB^{3+} were measured in the range of 21.3-33.5 and 21.3 and 35.4 at 20 Hz, respectively. For both series, the increasing dielectric constant up to 50 mol% B^{3+} concentration was associated with the developing grain size and crystallinity, while its decrease at 70 and 100 mol% was associated with the reduction in crystallite size. The dielectric loss factor for both series decreased with increasing B^{3+} concentration, whilst $Ba_2Gd_{1-x}TaO_6$:$x$$Eu^{3+}$, $y$$B^{3+}$ series exhibited a lower loss factor. The decline in dielectric loss in both series as B^{3+} concentration rises was linked to the reduction of oxygen vacancies. The heightened presence of B^{3+} resulted in diminished ionic conductivity and consequently decreased dielectric loss. The study may be useful in evaluating the dielectric properties of double perovskite ceramics, in terms of controlling the grain morphology and crystallite size.

5. CONFLICT OF INTEREST

There is no conflict of interest

6. REFERENCES

1. Luo Y, Chen Y, Li L, Chen J, Pang T, Chen L, et al. Three-mode fluorescence thermometers based on double perovskite Ba_2GdNbO_6:Eu^{3+},Mn^{4+} phosphors. Ceram Int [Internet]. 2023 Dec;49(23):38007–14. Available from: <URL>.

2. Li J, Wang X, Cui R, Deng C. Synthesis and photoluminescence studies of novel double-perovskite phosphors, Ba_2GdTaO_6:Eu^{3+} for WLEDs. Optik (Stuttg) [Internet]. 2020 Jan;201:163536. Available from: <URL>.

3. Sun Q, Wang S, Devakumar B, Sun L, Liang J, Huang X. Synthesis, Crystal Structure, and Photoluminescence Characteristics of High-Efficiency Deep-Red Emitting Ba_2GdTaO_6 :Mn^{4+} Phosphors. ACS Omega [Internet]. 2019 Aug 20;4(8):13474–80. Available from: <URL>.

4. Han B, Zhu J, Chu C, Yang X, Wang Y, Li K, et al. Sm^{3+}-Mn^{4+} activated Sr_2GdTaO_6 red phosphor for plant growth lighting and optical temperature sensing. Sensors Actuators A Phys [Internet]. 2023 Jan;349:114089. Available from: <URL>.

5. Sun J, Sun Z, Li Y, Jin Z, Ma L, Lu R, et al. Realization of plant growth lighting and temperature detecting based on novel Bi^{3+}, Sm^{3+} and Mn^{4+} doped Ca_2GdNbO_6 double perovskite phosphors. Opt Mater (Amst) [Internet]. 2023 Nov;145:114394. Available from: <URL>.

6. Wang L, Zhang Y, Gao D, Sha X, Chen X, Zhang Y, et al. Concentration- and temperature- dependent luminescence quenching and optical transition of Sr_2GdTaO_6: Eu^{3+} phosphor for potential applications in white LEDs. Results Phys [Internet]. 2024 Jan;56:107238. Available from: <URL>.

7. Han Y jie, Wang S, Liu H, Shi L, Zhang J ying, Zhang Z ni, et al. Synthesis and luminescent properties of a novel deep-red phosphor Sr_2GdNbO_6:Mn^{4+} for indoor plant growth lighting. J Lumin [Internet]. 2020 Apr;220:116968. Available from: <URL>.

8. Ranjbar B, Pavan A, Kennedy BJ, Zhang Z. Structural and magnetic properties of the ruthenium double perovskites $Ba_{2-x}Sr_xYRuO_6$. Dalt Trans [Internet]. 2015;44(23):10689–99. Available from: <URL>.

9. Shimizu Y, Sakagami S, Goto K, Nakachi Y, Ueda K. Tricolor luminescence in rare earth doped $CaZrO_3$ perovskite oxides. Mater Sci Eng B [Internet]. 2009 Apr;161(1–3):100–3. Available from: <URL>.

10. Wang S, Sun Q, Devakumar B, Liang J, Sun L, Huang X. Novel highly efficient and thermally stable Ca_2GdTaO_6:Eu^{3+} red-emitting phosphors with high color purity for UV/blue-excited WLEDs. J Alloys Compd [Internet]. 2019 Oct;804:93–9. Available from: <URL>.

11. Yin X, Wang Y, Huang F, Xia Y, Wan D, Yao J. Excellent red phosphors of double perovskite Ca_2LaMO_6:Eu (M=Sb, Nb, Ta) with distorted coordination environment. J Solid State Chem [Internet]. 2011 Dec;184(12):3324–8. Available from: <URL>.

12. Chen J, Zhao S, Zhao Z, Liao M, Pan S, Feng J, et al. The structure and luminescence properties of blue–green-emitting Sr_2YNbO_6: Bi^{3+} phosphors. J Lumin [Internet]. 2021 Nov;239:118336. Available from: <URL>.

13. Baral SC, Maneesha P, Rini EG, Sen S. Recent advances in LaNiMnO double perovskites for various applications; challenges and opportunities. Prog Solid State Chem [Internet]. 2023 Dec;72:100429. Available from: <URL>.

14. Wang CF, Shi C, Zheng A, Wu Y, Ye L, Wang N, et al. Achieving circularly polarized luminescence and large piezoelectric response in hybrid rare-earth double perovskite by a chirality induction strategy. Mater Horizons [Internet]. 2022;9(9):2450–9. Available from: <URL>.

15. Mishra S, Choudhary RNP, Parida SK. A multifunctional transition metal based double perovskite $Ba_2(FeW)O_6$: Structural, microstructural, optical, electrical and ferroelectric properties. Ceram Int [Internet]. 2023 Jul;49(14):22702–17. Available from: <URL>.

16. Parida BN, Panda N, Padhee R, Parida RK. Ferroelectric and optical behavior of $Pb_{0.5}Ba_{1.5}BiNbO_6$ double perovskite. Ferroelectrics [Internet]. 2019 Feb 17;540(1):18–28. Available from: <URL>.

17. Bendahhou A, Marchet P, El-Houssaine A, El Barkany S, Abou-Salama M. Relationship between structural and dielectric properties of Zn-substituted $Ba_5CaTi_{2-x}Zn_xNb_8O_{30}$ tetragonal tungsten bronze. CrystEngComm [Internet]. 2021;23(1):163–73. Available from: <URL>.

18. Jindal S, Vasishth A, Devi S, Anand G. A review on tungsten bronze ferroelectric ceramics as electrically tunable devices. Integr Ferroelectr [Internet]. 2018 Jan 2;186(1):1–9. Available from:

<URL>.

19. Shimizu K, Kato H, Kobayashi M, Kakihana M. Synthesis and photocatalytic properties of tetragonal tungsten bronze type oxynitrides. Appl Catal B Environ [Internet]. 2017 Jun;206:444–8. Available from: <URL>.

20. İlhan M, Keskin İÇ. Evaluation of structural behaviour, radioluminescence, Judd-Ofelt analysis and thermoluminescence kinetic parameters of Eu^{3+} doped TTB–type lead metaniobate phosphor. Phys B Condens Matter [Internet]. 2020 May;585:412106. Available from: <URL>.

21. İlhan M, Ekmekçi MK, Mergen A, Yaman C. Synthesis and Optical Characterization of Red-Emitting $BaTa_2O_6:Eu^{3+}$ Phosphors. J Fluoresc [Internet]. 2016 Sep 21;26(5):1671–8. Available from: <URL>.

22. İlhan M, Ekmekçi MK, Demir A, Demirer H. Synthesis and Optical Properties of Novel Red-Emitting $PbNb_2O_6$: Eu^{3+} Phosphors. J Fluoresc [Internet]. 2016 Sep 20;26(5):1637–43. Available from: <URL>.

23. İlhan M. Synthesis, structural characterization, and photoluminescence properties of TTB-type $PbTa_2O_6:Eu^{3+}$ phosphor. Int J Appl Ceram Technol [Internet]. 2017 Nov 30;14(6):1144–50. Available from: <URL>.

24. İlhan M, Güleryüz LF, Ekmekci MK. Structural Properties, Photoluminescence, and Judd-Ofelt Parameters of Eu^{3+}- Doped $CoNb_2O_6$ Phosphor. J Turkish Chem Soc Sect A Chem [Internet]. 2023 Aug 30;10(3):745–56. Available from: <URL>.

25. İlhan M, Ekmekçi MK, Keskin İÇ. Judd–Ofelt parameters and X-ray irradiation results of $MNb_2O_6:Eu^{3+}$ (M = Sr, Cd, Ni) phosphors synthesized *via* a molten salt method. RSC Adv [Internet]. 2021;11(18):10451–62. Available from: <URL>.

26. Başak AS, Ekmekçi MK, Erdem M, Ilhan M, Mergen A. Investigation of Boron-doping Effect on Photoluminescence Properties of $CdNb_2O_6$: Eu^{3+} Phosphors. J Fluoresc [Internet]. 2016 Mar 11;26(2):719–24. Available from: <URL>.

27. İlhan M, Katı Mİ, Keskin İÇ, Güleryüz LF. Evaluation of structural and spectroscopic results of tetragonal tungsten bronze $MTa_2O_6:Eu^{3+}$ (M = Sr, Ba, Pb) phosphors and comparison on the basis of Judd-Ofelt parameters. J Alloys Compd [Internet]. 2022 Apr;901:163626. Available from: <URL>.

28. İlhan M, Güleryüz LF. Boron doping effect on the structural, spectral properties and charge transfer mechanism of orthorhombic tungsten bronze β-$SrTa_2O_6:Eu^{3+}$ phosphor. RSC Adv [Internet]. 2023;13(18):12375–85. Available from: <URL>.

29. İlhan M, Güleryüz LF, Katı Mİ. Exploring the effect of boron on the grain morphology change and spectral properties of Eu^{3+} activated barium tantalate phosphor. RSC Adv [Internet]. 2024;14(4):2687–96. Available from: <URL>.

30. Li Z, Zhou W, Su X, Luo F, Huang Y, Wang C. Effect of boron doping on microwave dielectric properties of SiC powder synthesized by combustion synthesis. J Alloys Compd [Internet]. 2011 Jan;509(3):973–6. Available from: <URL>.

31. Mazumder R, Seal A, Sen A, Maiti HS. Effect of Boron Addition on the Dielectric Properties of Giant Dielectric $CaCu_3Ti_4O_{12}$ Ferroelectrics [Internet]. 2005 Oct;326(1):103–8. Available from: <URL>.

32. Zhang X, Wang B, Huang W, Chen Y, Wang G, Zeng L, et al. Synergistic Boron Doping of Semiconductor and Dielectric Layers for High-Performance Metal Oxide Transistors: Interplay of Experiment and Theory. J Am Chem Soc [Internet]. 2018 Oct 3;140(39):12501–10. Available from: <URL>.

33. Cullity BD, Stock SR. Elements of X-ray Diffraction. USA: Prentice Hall; 2001.

34. Koshy J, Thomas JK, Kurian J, Yadava YP, Damodaran AD. Development and characterization of $GdBa_2NbO_6$, a new ceramic substrate for YBCO thick films. Mater Lett [Internet]. 1993 Oct;17(6):393–7. Available from: <URL>.

35. Babu TGN, Koshy J. Ba_2GdTaO_6, a ceramic substrate for $YBa_2Cu_3O_7$−gd films. Mater Lett [Internet]. 1997 Nov;33(1–2):7–11. Available from: <URL>.

36. Tahar RBH, Tahar NBH. Boron-doped zinc oxide thin films prepared by sol-gel technique. J Mater Sci [Internet]. 2005 Oct;40(19):5285–9. Available from: <URL>.

37. Addonizio ML, Diletto C. Doping influence on intrinsic stress and carrier mobility of LP-MOCVD-deposited ZnO:B thin films. Sol Energy Mater Sol Cells [Internet]. 2008 Nov;92(11):1488–94. Available from: <URL>.

38. İlhan M, Ekmekçi MK, Güleryüz LF. Effect of boron incorporation on the structural, morphological, and spectral properties of $CdNb_2O_6:Dy^{3+}$ phosphor synthesized by molten salt process. Mater Sci Eng B [Internet]. 2023 Dec;298:116858. Available from: <URL>.

39. Polyxeni V, Nikolaos D P, Nikos S, Sotirios X, Evangelos H. Temperature effects on grain growth phenomena and magnetic properties of silicon steels used in marine applications. Ann Mar Sci [Internet]. 2023 Jun 21;7(1):40–4. Available from: <URL>.

40. Güleryüz LF, İlhan M. Structural, morphological, spectral properties and high quantum efficiency of Eu^{3+}, B^{3+} co-activated double perovskite Ba_2GdMO_6 (M = Nb, Ta) phosphors. Mater Sci Eng B [Internet]. 2024 Jun;304:117373. Available from: <URL>.

41. Mahapatro J, Agrawal S. Effect of Eu^{3+} ions on electrical and dielectric properties of barium hexaferrites prepared by solution combustion method. Ceram Int [Internet]. 2021 Jul;47(14):20529–43. Available from: <URL>.

42. Evangeline T G, Annamalai A R, Ctibor P. Effect of Europium Addition on the Microstructure and Dielectric Properties of CCTO Ceramic Prepared Using Conventional and Microwave Sintering. Molecules [Internet]. 2023 Feb 8;28(4):1649. Available from: <URL>.

43. Rayssi C, El.Kossi S, Dhahri J, Khirouni K. Frequency and temperature-dependence of dielectric permittivity and electric modulus studies of the solid solution $Ca_{0.85}Er_{0.1}Ti_{1-x}Co_{4x/3}O_3(0\leq x\leq 0.1)$. RSC Adv [Internet]. 2018;8(31):17139–50. Available from: <URL>.

44. Kadam AA, Shinde SS, Yadav SP, Patil PS, Rajpure KY. Structural, morphological, electrical and magnetic properties of Dy doped Ni–Co substitutional spinel ferrite. J Magn Magn Mater [Internet]. 2013 Mar;329:59–64. Available from: <URL>.

45. Tan YQ, Yu Y, Hao YM, Dong SY, Yang YW. Structure and dielectric properties of $Ba_5NdCu_{1.5}Nb_{8.5}O_{30-\delta}$ tungsten bronze ceramics. Mater Res Bull [Internet]. 2013 May;48(5):1934–8. Available from: <URL>.

46. Esha IN, Al-Amin M, Toma FTZ, Hossain E, Khan MNI, Maria KH. Synthesis and analysis of the influence of Eu^{3+} on the structural, ferromagnetic, dielectric and conductive characteristics of $Ni0.4Zn_{0.45}Cu_{0.15}Fe_{(2-x)}Eu_xO_4$ composites using conventional double sintering ceramic method. J Ceram Process Res [Internet]. 2019 Oct;20(5):530–9. Available from: <URL>.

47. Shah MR, Akther Hossain AKM. Structural and dielectric properties of La substituted polycrystalline $Ca(Ti_{0.5}Fe_{0.5})O_3$. Mater Sci [Internet]. 2013 Jan 25;31(1):80–7. Available from: <URL>.

48. Wagner KW. Zur Theorie der unvollkommenen Dielektrika. Ann Phys [Internet]. 1913 Jan 14;345(5):817–55. Available from: <URL>.

49. Maxwell JC. A treatise on electricity and magnetism. London: Caleredon press, Oxford University; 1873.

50. Samet M, Kallel A, Serghei A. Maxwell-Wagner-Sillars interfacial polarization in dielectric spectra of composite materials: Scaling laws and applications. J Compos Mater [Internet]. 2022 Aug 28;56(20):3197–217. Available from: <URL>.

51. Saengvong P, Chanlek N, Srepusharawoot P, Harnchana V, Thongbai P. Enhancing giant dielectric properties of Ta^{5+} -doped $Na_{1/2}Y_{1/2}Cu_3Ti_4O_{12}$ ceramics by engineering grain and grain boundary. J Am Ceram Soc [Internet]. 2022 May 15;105(5):3447–55. Available from: <URL>.

52. Karmakar S, Mohanty HS, Behera D. Exploration of alternating current conduction mechanism and dielectric relaxation with Maxwell–Wagner effect in NiO–CdO–Gd_2O_3 nanocomposites. Eur Phys J Plus [Internet]. 2021 Oct 15;136(10):1038. Available from: <URL>.

53. Caruntu G, Rarig Jr R, Dumitru I, O’Connor CJ. Annealing effects on the crystallite size and dielectric properties of ultrafine $Ba_{1-x}Sr_xTiO_3(0<x<1)$ powders synthesized through an oxalate-complex precursor. J Mater Chem [Internet]. 2006;16(8):752–8. Available from: <URL>.

54. Kim L, Jung D, Kim J, Kim YS, Lee J. Strain manipulation in $BaTiO_3/SrTiO_3$ artificial lattice toward high dielectric constant and its nonlinearity. Appl Phys Lett [Internet]. 2003 Mar 31;82(13):2118–20. Available from: <URL>.

55. Sati PC, Kumar M, Chhoker S, Jewariya M. Influence of Eu substitution on structural, magnetic, optical and dielectric properties of $BiFeO_3$ multiferroic ceramics. Ceram Int [Internet]. 2015 Mar;41(2):2389–98. Available from: <URL>.

56. Ganguly P, Jha AK. Enhanced characteristics of $Ba_5SmTi_3Nb_7O_{30}$ ferroelectric nanocrystalline ceramic prepared by mechanical activation process: A comparative study. Mater Res Bull [Internet]. 2011 May;46(5):692–7. Available from: <URL>.

57. Iqbal MJ, Yaqub N, Sepiol B, Ismail B. A study of the influence of crystallite size on the electrical and magnetic properties of $CuFe_2O_4$. Mater Res Bull [Internet]. 2011 Nov;46(11):1837–42. Available from: <URL>.

58. Chakrabarti A, Bera J. Effect of La-substitution on the structure and dielectric properties of $BaBi_4Ti_4O_{15}$ ceramics. J Alloys Compd [Internet]. 2010 Sep;505(2):668–74. Available from: <URL>.

59. Kumar P, Kar M. Effect of structural transition on magnetic and optical properties of Ca and Ti co-substituted $BiFeO_3$ ceramics. J Alloys Compd [Internet]. 2014 Jan;584:566–72. Available from: <URL>.

60. İlhan M, Ekmekci MK, Esmer K. Structural and dielectric properties of Eu^{3+},B^{3+} co-doped $CoNb_2O_6$ ceramic. J Turkish Chem Soc Sect A Chem [Internet]. 2024 May 15;11(2):765–74. Available from: <URL>.

61. Kendall KR, Thomas JK, Loye HC. Synthesis and ionic conductivity of a new series of modified Aurivillius phases. Chem Mater [Internet]. 1995 Jan 1;7(1):50–7. Available from: <URL>.

62. Fei Liu S, Jun Wu Y, Li J, Ming Chen X. Effects of oxygen vacancies on dielectric, electrical, and ferroelectric properties of $Ba_4Nd_2Fe_2Nb_8O_{30}$ ceramics. Appl Phys Lett [Internet]. 2014 Feb 24;104(8):082912. Available from: <URL>.